Electronic Supplementary Material (ESI) for Journal of Materials Chemistry A.

Supplementary information (ESI) for Journal of Materials Chemistry

General solution-processed formation of porous transition-metal oxides on exfoliated molybdenum disulfides for high-performance asymmetric supercapacitors†

Kai Wang,[a] Jing Yang,[a] Jixin Zhu,[b] Le Li,[a] Ying Liu,[a] Chao Zhang*[a] and Tianxi Liu*[a]

[a] State Key Laboratory for Modification of Chemical Fibers and Polymer Materials, College of Materials Science and Engineering, Donghua University, Shanghai 201620, P. R. China

[b] Key Laboratory of Flexible Electronics (KLOFE) & Institute of Advanced Materials (IAM), Jiangsu National Synergetic Innovation Center for Advanced Materials (SICAM), Nanjing Tech University (NanjingTech), 30 South Puzu Road, Nanjing 211816, China

* E-mail: czhang@dhu.edu.cn (C. Zhang)

* E-mail: txliu@fudan.edu.cn or txliu@dhu.edu.cn (T. X. Liu)

Electronic Supplementary Information

Figure caption:

Fig. S1. (a) Digital images showing the as-obtained (left) and diluted (right) suspension of f-MoS_2 in NMP. (b) Digital images showing the as-obtained (left) and diluted (right) suspension of f-MoS_2 in DI water upon the solvent-exchange method.

Fig. S2. The direct sonication of b-MoS_2 in water cannot produce exfoliated f-MoS_2 suspension.

Fig. S3. (a) Nitrogen sorption isotherms and (b) pore size distributions for $Ni(OH)_2$ and NiO. (c) Nitrogen sorption isotherms and (d) pore size distributions for MoS_2-NiO, MoS_2-$Ni(OH)_2$ and f-MoS_2.

Fig. S4. (a) XRD patterns of b-MoS_2 and f-MoS_2. (b) XRD patterns of MoS_2-$Ni(OH)_2$, $Ni(OH)_2$ and f-MoS_2.

Fig. S5. XPS spectra of (a) survey and (b) O 1s of the MoS_2-NiO-2 sample.

Fig. S6. SEM image of b-MoS_2.

Fig. S7. TEM images of f-MoS_2 at (a) low and (b) high magnifications, respectively.

Fig. S8. SEM images of (a, b) MoS_2-NiO-1 and (c, d) MoS_2-NiO-3 at low and high magnifications, respectively.

Fig. S9. SEM images of NiO at (a) low and (b) high magnifications, respectively.

Fig. S10. SEM image and the corresponding elemental mappings of MoS_2-NiO-2 sample.

Fig. S11. TEM images of MoS_2-Co_3O_4 at different magnifications.

Fig. S12. SEM images of Co_3O_4 at (a) low and (b) high magnifications, respectively.

Fig. S13. (a) XRD patterns of MoS_2-$Co(OH)_2$, $Co(OH)_2$ and f-MoS_2. (b) XRD patterns of MoS_2-Co_3O_4, Co_3O_4 and f-MoS_2.

Fig. S14. TEM image of MoS_2-Fe_2O_3 at low magnification.

Fig. S15. SEM images of Fe_2O_3 at (a) low and (b) high magnifications, respectively.

Fig. S16. XRD patterns of MoS_2-Fe_2O_3, Fe_2O_3 and f-MoS_2 before (a) and after (b) annealing.

Fig. S17. Comparison of CV curves of graphite paper current collector and MoS_2-NiO-2 at a scan rate of 50 mV s^{-1}.

Fig. S18. (a) CV curves of NiO at various scan rates, and (b) plot of the current densities of the cathodic peak for the MoS_2-NiO-2 and NiO electrodes as functions of the square roots of the scan rates.

Fig. S19. CV curves of (a) MoS_2-NiO-2, (b) f-MoS_2, and (c) NiO electrodes in electrochemical double-layer region at scan rates of 5, 10, 20, 50, 75 and 100 mV s^{-1}. (d) The ratio of the discharge current at 0.05 V with various scan rates of MoS_2-NiO-2, f-MoS_2, and NiO electrodes.

Fig. S20. Comparison of galvanostatic charge/discharge curves of MoS_2-NiO, NiO and f-MoS_2 at a current density of 0.5 A g^{-1}.

Fig. S21. Comparison of galvanostatic charge/discharge curves of MoS_2-NiO-2 at various current densities.

Fig. S22. Nyquist plots of MoS_2-NiO, NiO and f-MoS_2 electrodes in the frequency ranging from 1 MHz to 0.01 Hz (inset is the enlargement of the high-frequency region).

Fig. S23. (a) Comparison of CV curves of MoS_2-Co_3O_4, Co_3O_4 and f-MoS_2 at 5 mV s^{-1}. (b) CV curves of MoS_2-Co_3O_4 at different scan rates. (c) Specific capacitances of MoS_2-Co_3O_4, Co_3O_4 and f-MoS_2 at various current densities. (d) Cycling performance of MoS_2-Co_3O_4 and Co_3O_4 at 2 A g^{-1}.

Fig. S24. CV curves of (a) f-MoS_2 and (b) Co_3O_4 at different scan rates, and the galvanostatic discharge curves of (c) f-MoS_2, (d) Co_3O_4 and (e) MoS_2-Co_3O_4 at different current densities.

Fig. S25. CV curves of (a) f-MoS_2, (b) Fe_2O_3 and (c) MoS_2-Fe_2O_3 at different scan rates. Galvanostatic charge/discharge curves of (d) f-MoS_2, (e) Fe_2O_3 and (f) MoS_2-Fe_2O_3 at different current densities.

Fig. S26. (a) Comparison of CV curves of MoS_2-Fe_2O_3, Fe_2O_3 and f-MoS_2 at a scan rate of 5 mV s^{-1}. (b) Specific capacitances of MoS_2-Fe_2O_3, Fe_2O_3 and f-MoS_2 at various current densities. (c) Cycling performance of MoS_2-Fe_2O_3 and Fe_2O_3 at a current density of 2 A g^{-1}.

Table S1. The BET surface areas and pore size distributions of $Ni(OH)_2$ and MoS_2-$Ni(OH)_2$.

Samples	S_{BET} [m^2 g^{-1}]	Total pore volume [mL g^{-1}]	Micropore volume [mL g^{-1}]	Mesopore volume [mL g^{-1}]
$Ni(OH)_2$	39.9	0.10	~ 0	0.10
MoS_2-$Ni(OH)_2$	45.6	0.14	~ 0	0.14

Table S2. Comparison of electrochemical capacitive performances of MoS_2-NiO hybrids with NiO-based hybrids in other literatures.

Electrode materials	**Specific capacitance ($F g^{-1}$)**		**Ref.**
	1 $A g^{-1}$	**20 $A g^{-1}$**	
NiO@PPy	595	401.2	[S1]
NiO nanotube arrays	523.4	230.1	[S2]
MoS_2@$Ni(OH)_2$	657	242.2	[S3]
MoS_2@PANI	864.5	263.2	[S4]
NiO coated graphene/PANI	1260.2	521	[S5]
CNT arrays@NiO	1120.2	385.2	[S6]
CNT@NiO	1098.4	516.8	[S7]
MoS_2-NiO-2	**1080.6**	**668.4**	**This work**

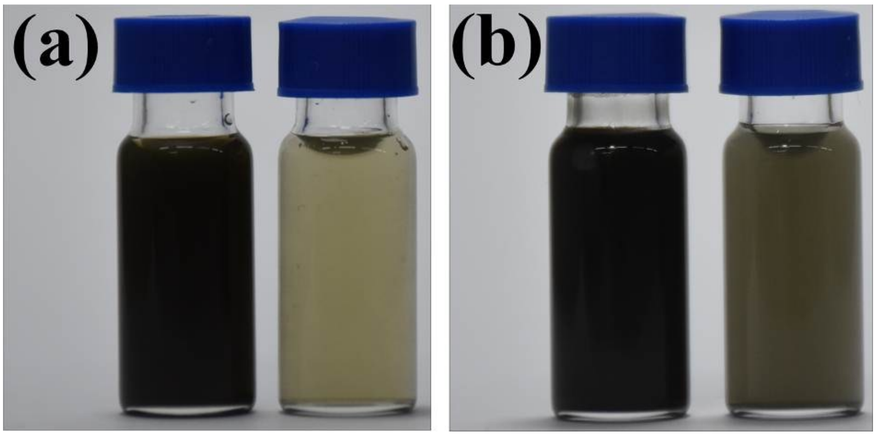

Fig. S1. (a) Digital images showing the as-obtained (left) and diluted (right) suspension of f-MoS_2 in NMP. All the two samples are left standing for 2 weeks before taking the photograph. (b) Digital images showing the as-obtained (left) and diluted (right) suspension of f-MoS_2 in DI water upon the solvent-exchange method, which are left standing for 24 h before taking the photograph.

Fig. S2. The direct sonication of b-MoS_2 in water cannot produce exfoliated f-MoS_2 suspension.

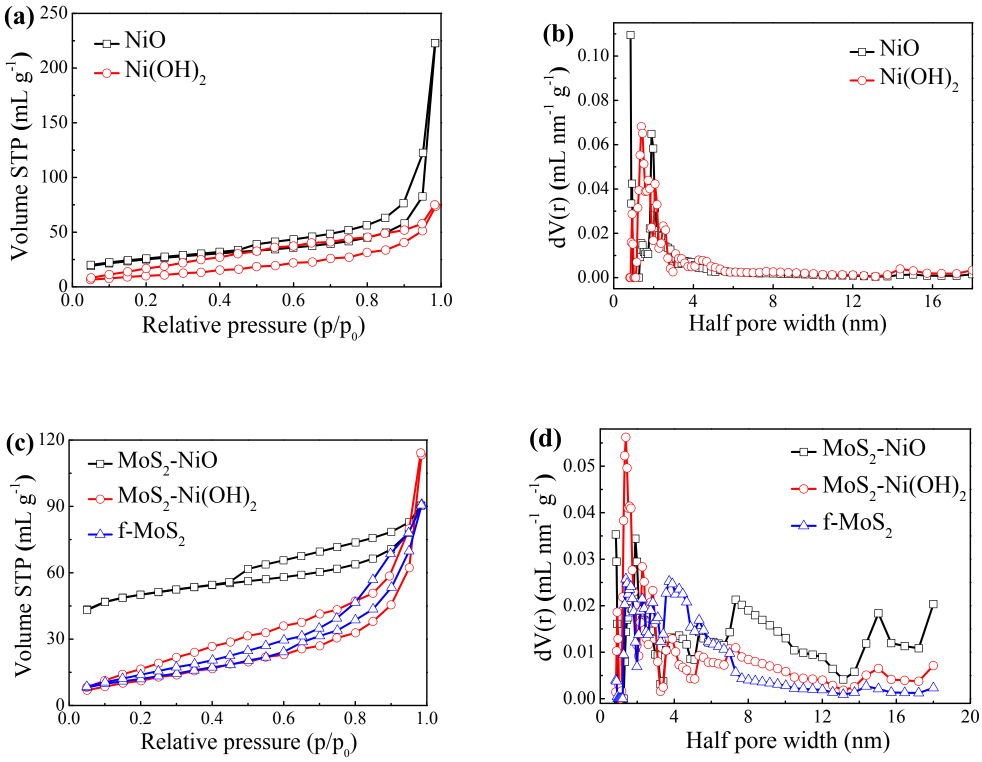

Fig. S3. (a) Nitrogen sorption isotherms and (b) pore size distributions for $Ni(OH)_2$ and NiO. (c) Nitrogen sorption isotherms and (d) pore size distributions for MoS_2-NiO, MoS_2-$Ni(OH)_2$ and f-MoS_2.

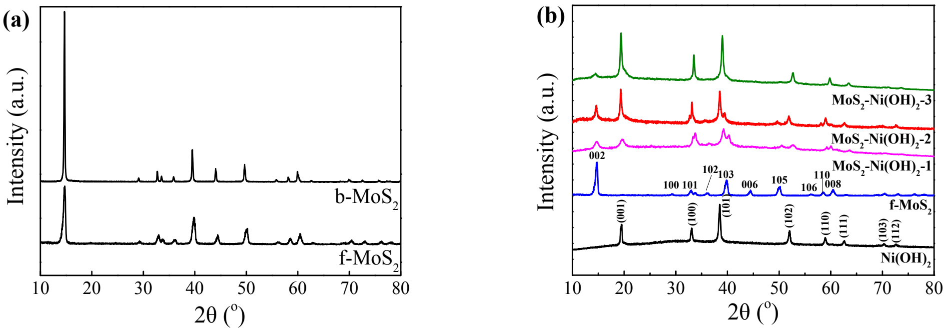

Fig. S4. (a) XRD patterns of b-MoS$_2$ and f-MoS$_2$. (b) XRD patterns of MoS$_2$-Ni(OH)$_2$, Ni(OH)$_2$ and f-MoS$_2$. For the intermediates of MoS$_2$-Ni(OH)$_2$ hybrids, Ni(OH)$_2$ shows XRD patterns centered at 2θ = 18.5, 31.3, 38.8, 51.5, 58.3, 62.1, 69.7 and 71.9°, which can be ascribed to the (002), (100), (101), (102), (110), (111), (103) and (112) planes, respectively, validating the formation of α-phase hexagonal structure of Ni(OH)$_2$ (JCPDS card No.14-0117).

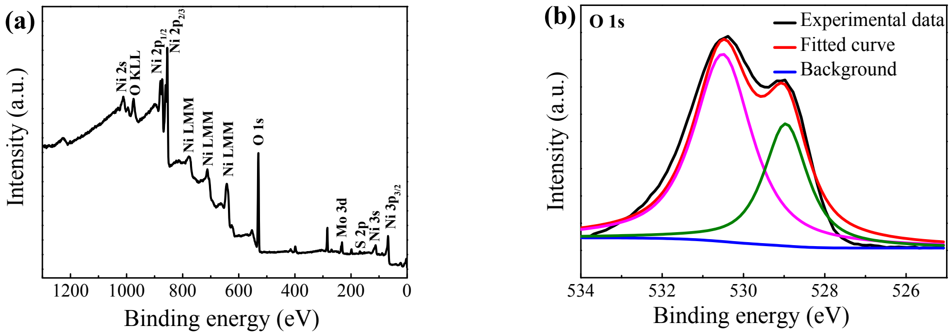

Fig. S5. XPS spectra of (a) survey and (b) O 1s of the MoS_2-NiO-2 sample. A binding energy peak at 529.0 eV corresponds to O atoms from NiO, while the peak located at 530.5 eV can be ascribed to the absorbed O_x^- ions (O^- and O_2^- ions) in the oxygen-deficient regions within the NiO.

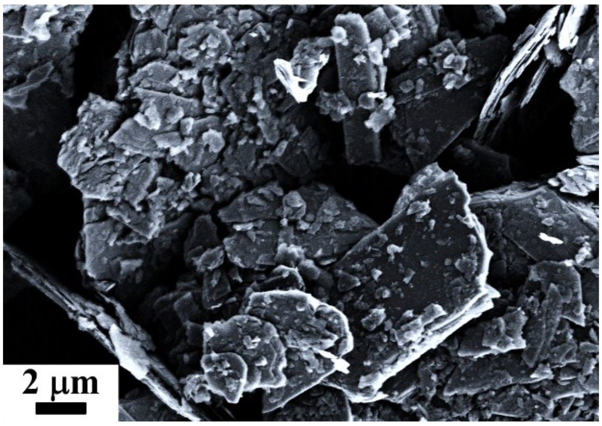

Fig. S6. SEM image of b-MoS_2.

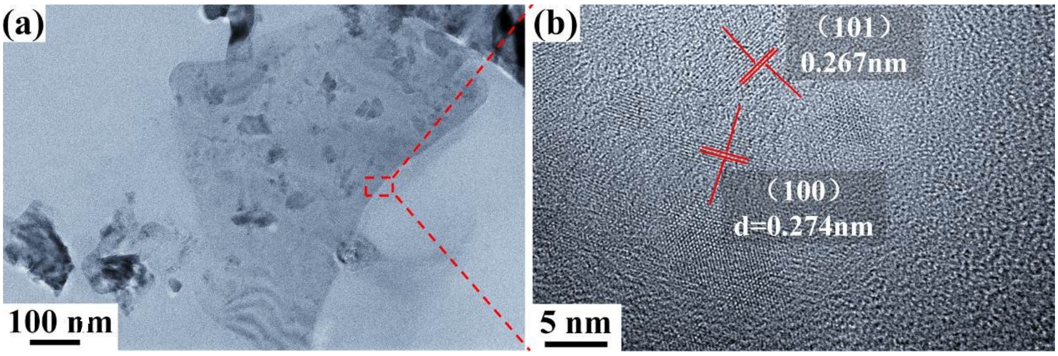

Fig. S7. TEM images of f-MoS_2 at (a) low and (b) high magnifications, respectively.

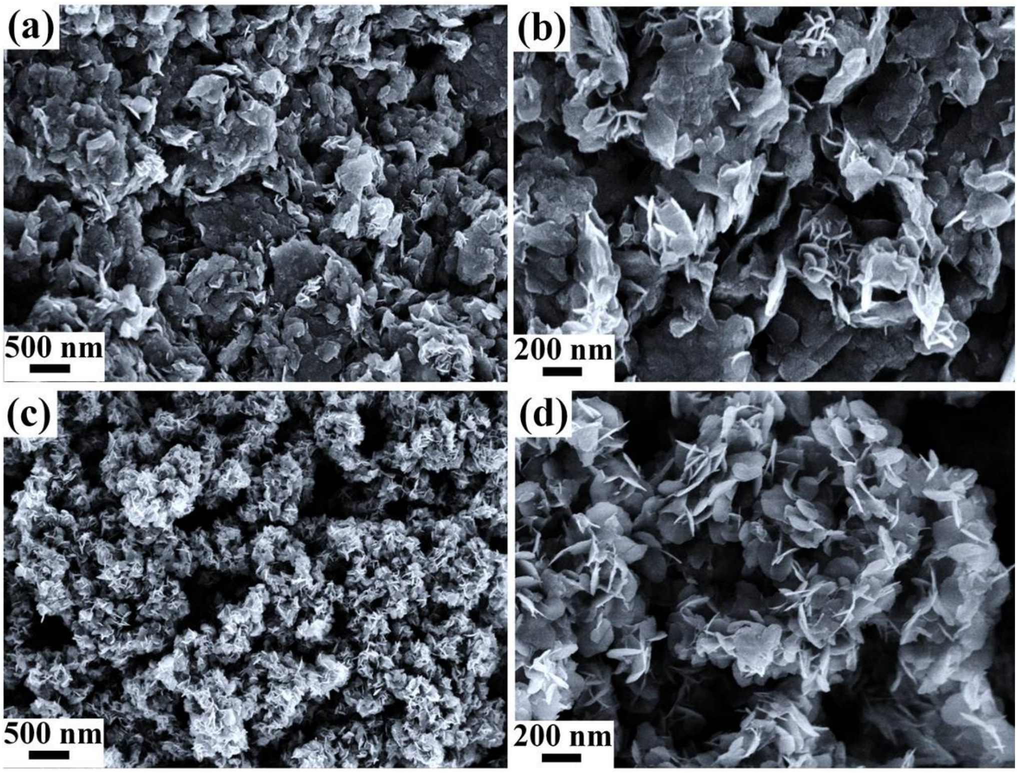

Fig. S8. SEM images of (a, b) MoS_2-NiO-1 and (c, d) MoS_2-NiO-3 at low and high magnifications, respectively.

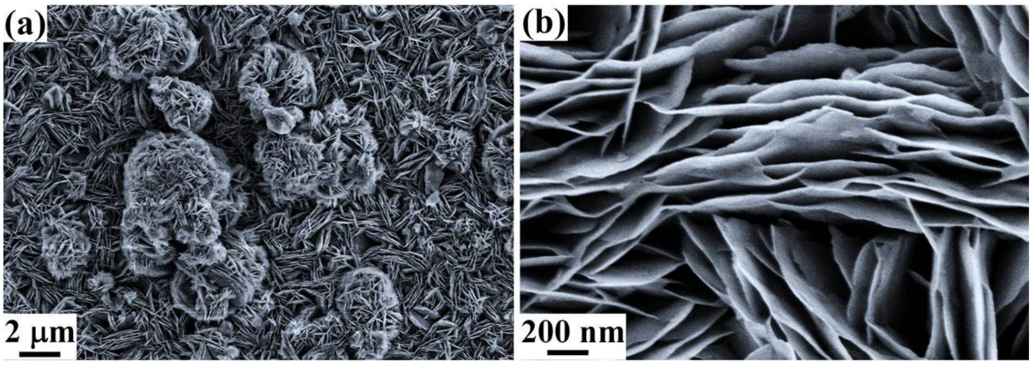

Fig. S9. SEM images of NiO at (a) low and (b) high magnifications, respectively.

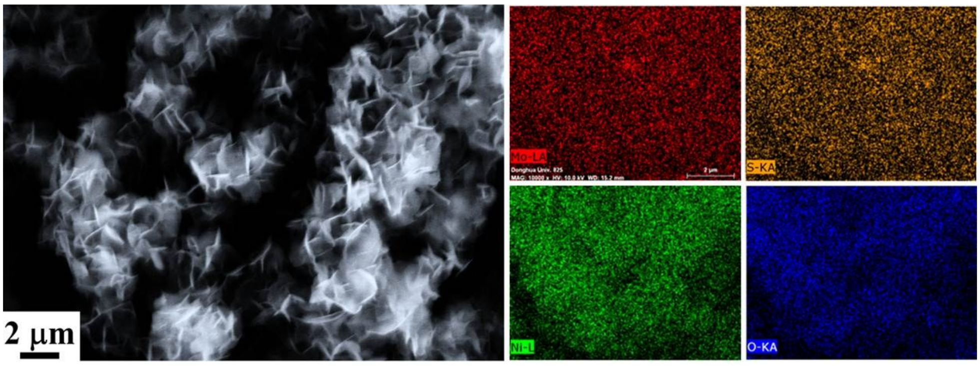

Fig. S10. SEM image and the corresponding elemental mappings of MoS_2-NiO-2 sample.

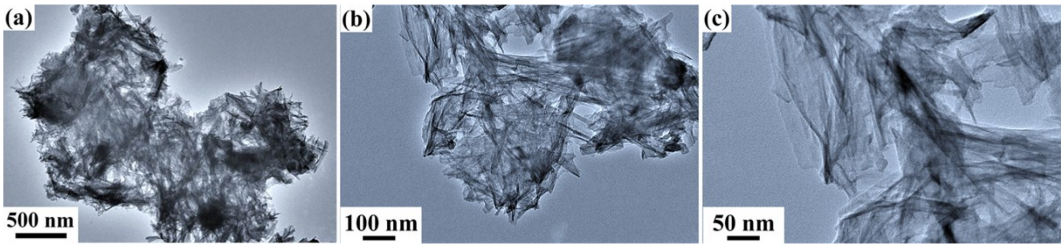

Fig. S11. TEM images of MoS_2-Co_3O_4 hybrid at different magnifications.

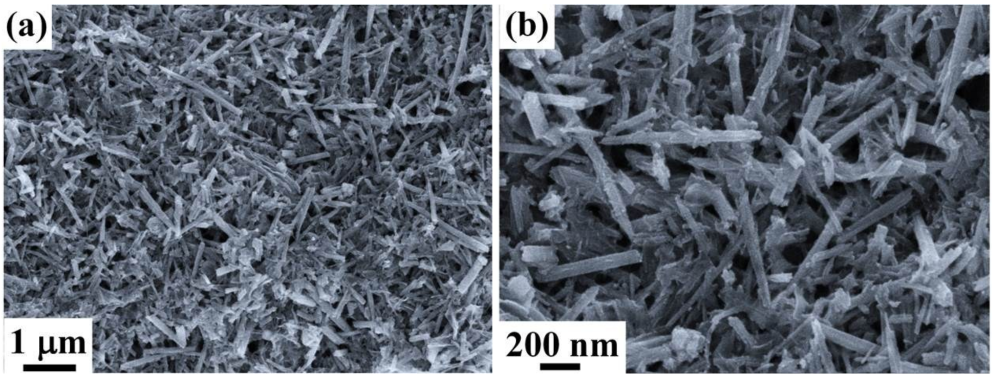

Fig. S12. SEM images of Co_3O_4 at (a) low and (b) high magnifications, respectively, which show a nanowire morphology (50 ~ 70 nm in diameter; ~ 500 nm in length) with staggered distributions.

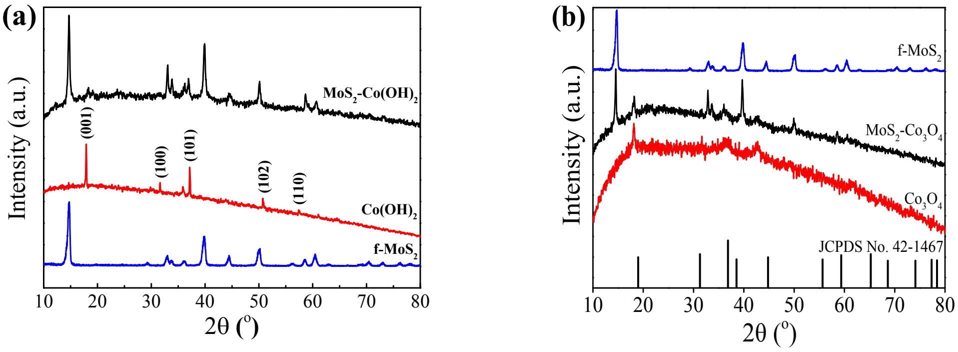

Fig. S13. (a) XRD patterns of MoS_2-$Co(OH)_2$, $Co(OH)_2$ and f-MoS_2. (b) XRD patterns of MoS_2-Co_3O_4, Co_3O_4 and f-MoS_2. The diffraction peaks of the as-obtained products with sharp and slender peaks are well indexed into brucite β-$Co(OH)_2$ (JCPDS card No. 45-0031) for the intermediates and cubic Co_3O_4 (JCPDS card No. 42-1467) for the final products, which imply their good crystallinity within the hybrids.

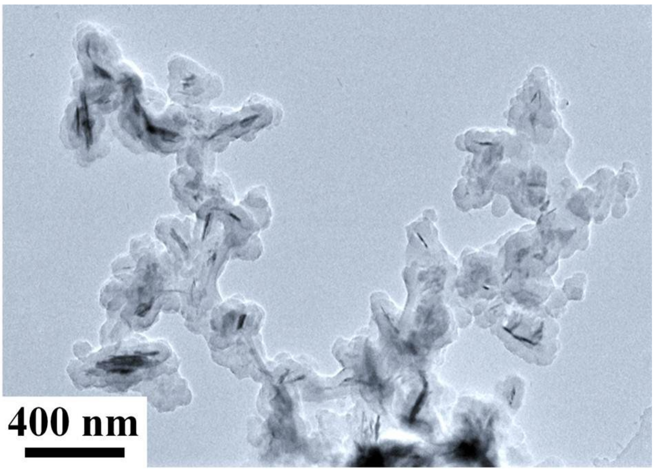

Fig. S14. TEM image of MoS_2-Fe_2O_3 at low magnification.

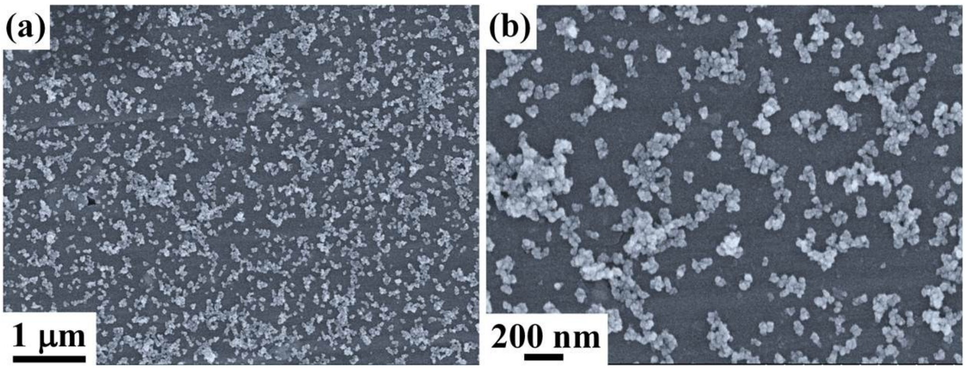

Fig. S15. SEM images of Fe_2O_3 at (a) low and (b) high magnifications, respectively. Neat Fe_2O_3 shows a nanoparticle morphology with a uniform size.

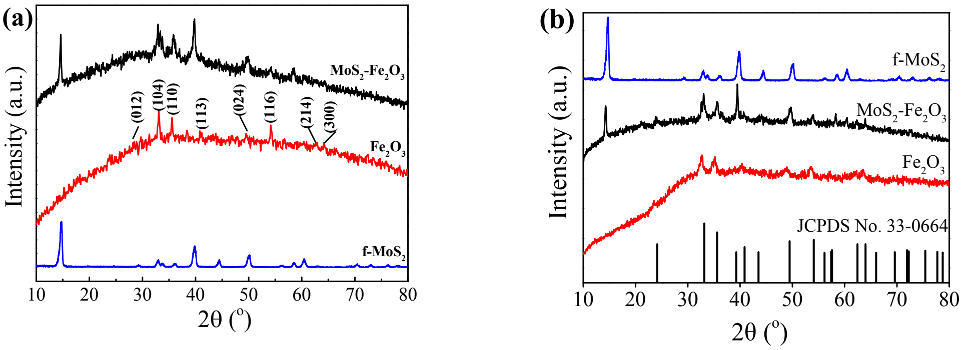

Fig. S16. XRD patterns of MoS_2-Fe_2O_3, Fe_2O_3 and f-MoS_2 before (a) and after (b) annealing. XRD patterns of MoS_2-Fe_2O_3 hybrids before and after annealing are both indexed well with that of monoclinic Fe_2O_3 (JCPDS no. 33-0664). This might be due to the instability of the $Fe(OH)_3$, which will be directly converted into Fe_2O_3 during the reaction process, but the post-annealing process makes the Fe_2O_3 in the hybrids with higher crystallinity.

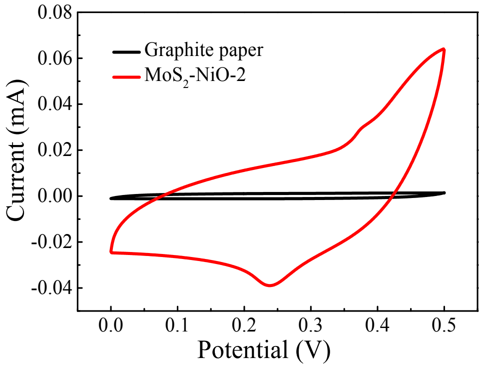

Fig. S17. Comparison of CV curves of graphite paper current collector and MoS_2-NiO-2 at a scan rate of 50 mV s^{-1}.

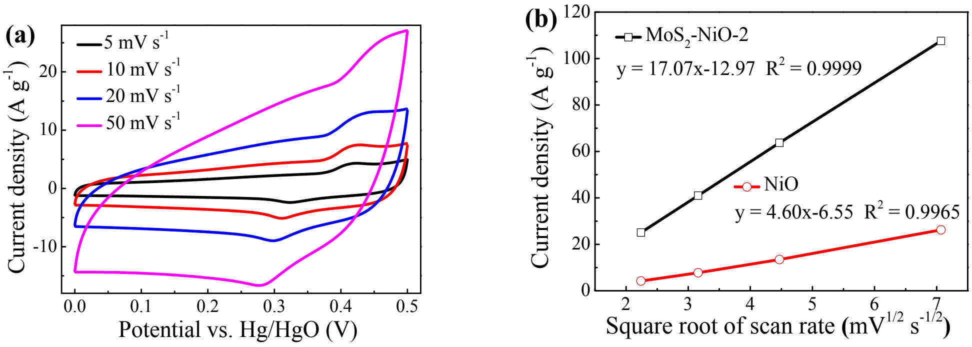

Fig. S18. (a) CV curves of NiO at various scan rates, and (b) plot of the current densities of the cathodic peak for the MoS_2-NiO-2 and NiO electrodes as functions of the square roots of the scan rates.

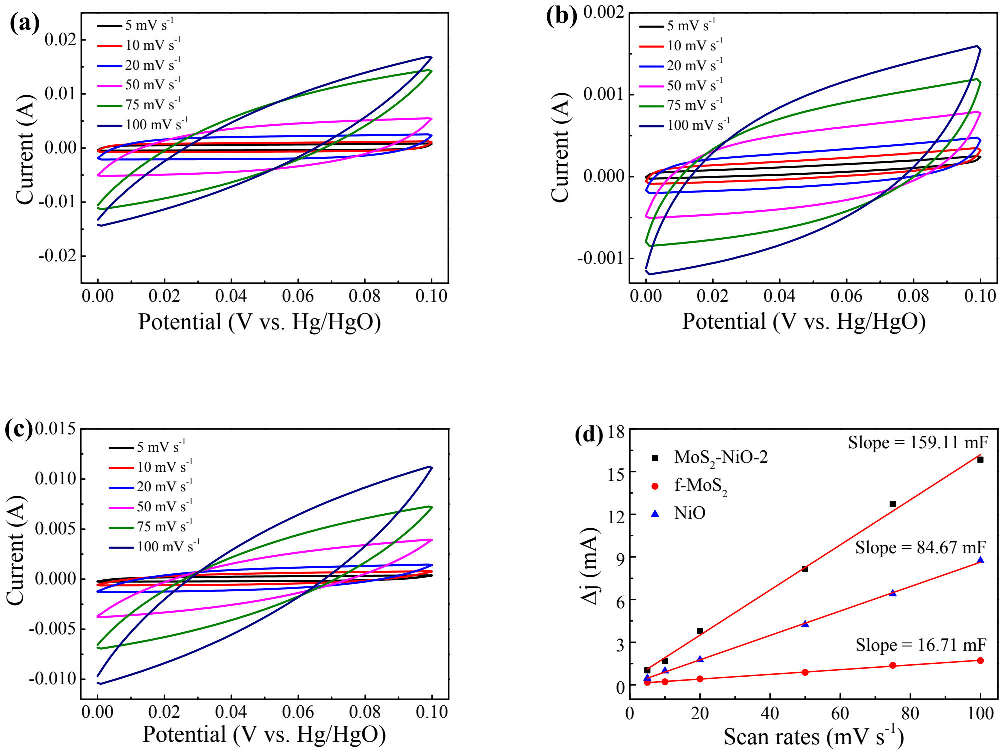

Fig. S19. CV curves of (a) MoS_2-NiO-2, (b) f-MoS_2, and (c) NiO electrodes in electrochemical double-layer region at scan rates of 5, 10, 20, 50, 75 and 100 mV s^{-1}. (d) The ratio of the discharge current at 0.05 V with various scan rates of MoS_2-NiO-2, f-MoS_2, and NiO electrodes.

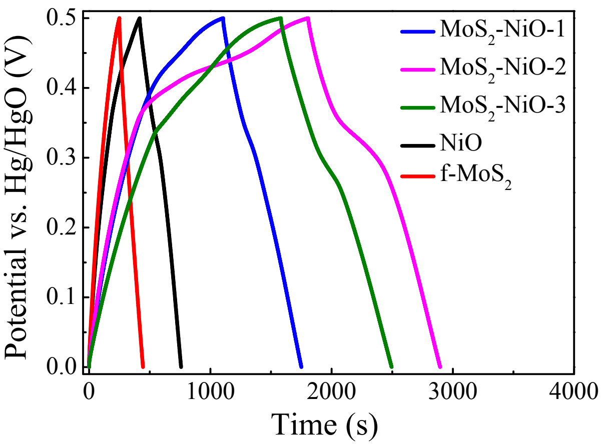

Fig. S20. Comparison of galvanostatic charge/discharge curves of MoS_2-NiO, NiO and f-MoS_2 at a current density of 0.5 A g^{-1}. For the NiO and MoS_2-NiO electrodes, two variation regions are observed in the charge/discharge curves, in which a linear variation of potential/time dependence (below ~ 0.37 V) indicates an entire double layer capacitive behavior from the charge separation at the electrode/electrolyte interface. By contrast, a potential plateau of potential vs. time (0.25 ~ 0.35 V) indicates a typical pseudocapacitive behavior, which is caused by a redox reaction at the electrode/electrolyte interface. Meanwhile, the ideal straight line for the f-MoS_2 electrode demonstrates a typical double layer capacitive behavior.

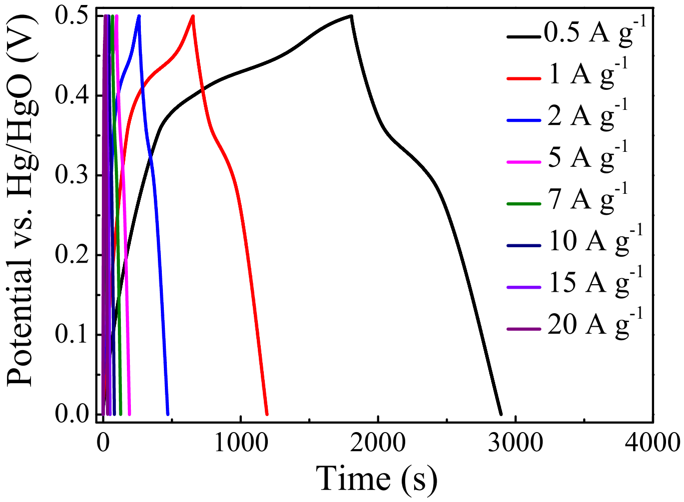

Fig. S21. Comparison of galvanostatic charge/discharge curves of MoS_2-NiO-2 at various current densities. The potential plateau can be observed in all charge/discharge curves which are in good accordance with the data from the CV measurements. The specific capacitances are calculated by the following equation:

$$C = \frac{It}{mV}$$

where I is the charge/discharge current, t is the discharge time, V is the voltage range, and m is the mass of the active materials in the electrode.

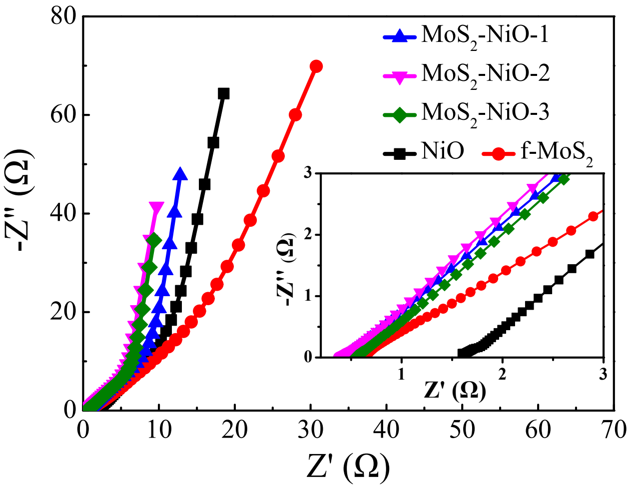

Fig. S22. Nyquist plots of MoS_2-NiO, NiO and f-MoS_2 electrodes in the frequency ranging from 1 MHz to 0.01 Hz (inset is the enlargement of the high-frequency region). No semicircles can be observed in high-frequency regions for all the electrodes, indicating extremely low charge-transfer resistances (R_{ct}) of the Faradaic process for all electrodes. The intercept of the curve at Z′-axis at the high frequency demonstrates the resistance of the electrochemical system (R_s, which includes the intrinsic resistance of the substrate, the ionic resistance of electrolyte, and the contact resistance between current collector and active material). The MoS_2-NiO-2 electrode displays the lowest R_s (0.38 Ω) among all the electrodes (0.42, 0.55, 0.65 and 1.6 Ω for MoS_2-NiO-1, MoS_2-NiO-3, f-MoS_2 and NiO, respectively), suggesting that the MoS_2-NiO-2 electrode owns a lower internal resistance. MoS_2-NiO-2 electrode shows a more ideal linear in the low-frequency region, which indicates a more efficient electrolyte and proton diffusion. The above results distinctly demonstrate that the rational construction of heterostructured MoS_2-NiO electrode shows the favorable charge-transfer kinetics, the full utilization of the electroactive materials, and the expedite penetration of the electrolyte within the electrode, which adequately explain the increase of the electrochemical performances of the as-synthesized hybrids as described above.

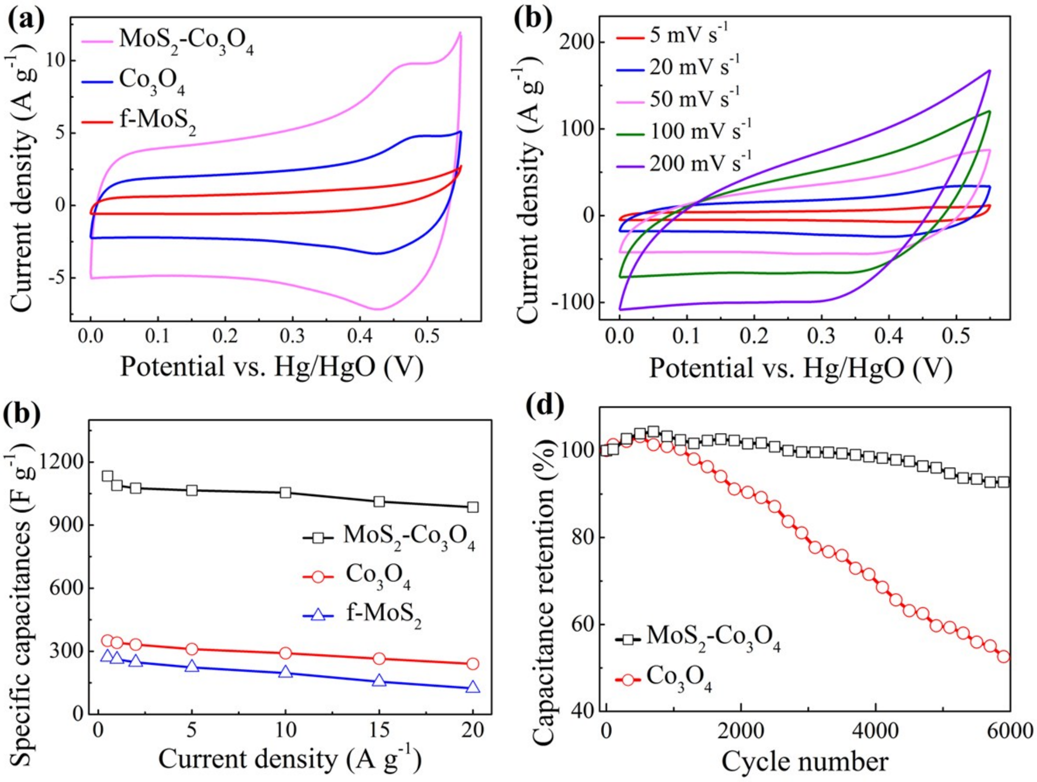

Fig. S23. (a) Comparison of CV curves of MoS_2-Co_3O_4, Co_3O_4 and f-MoS_2 at 5 mV s^{-1}. (b) CV curves of MoS_2-Co_3O_4 at different scan rates. (c) Specific capacitances of MoS_2-Co_3O_4, Co_3O_4 and f-MoS_2 at various current densities. (d) Cycling performance of MoS_2-Co_3O_4 and Co_3O_4 at 2 A g^{-1}.

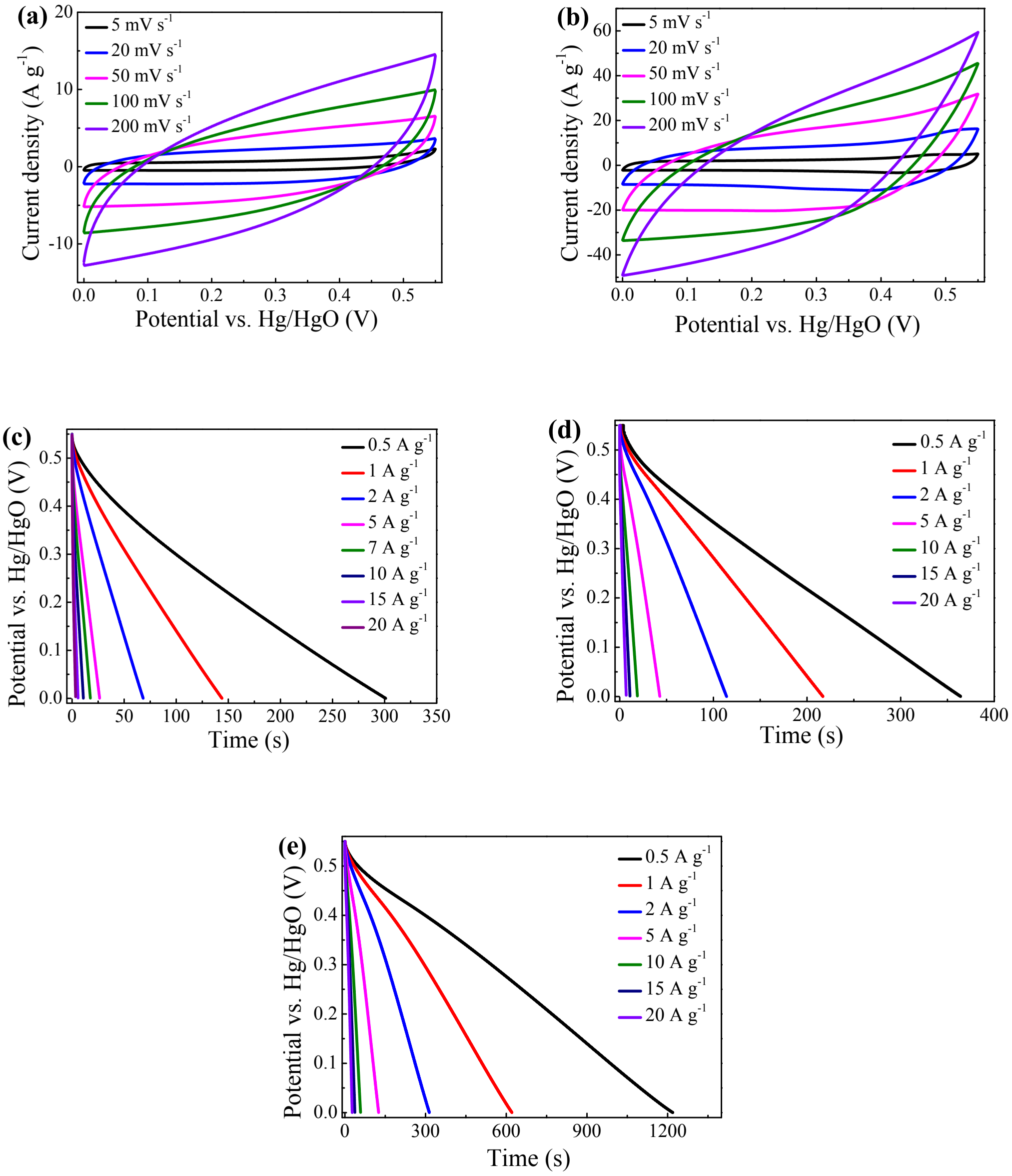

Fig. S24. CV curves of (a) f-MoS_2 and (b) Co_3O_4 at different scan rates, and the galvanostatic discharge curves of (c) f-MoS_2, (d) Co_3O_4 and (e) MoS_2-Co_3O_4 at different current densities.

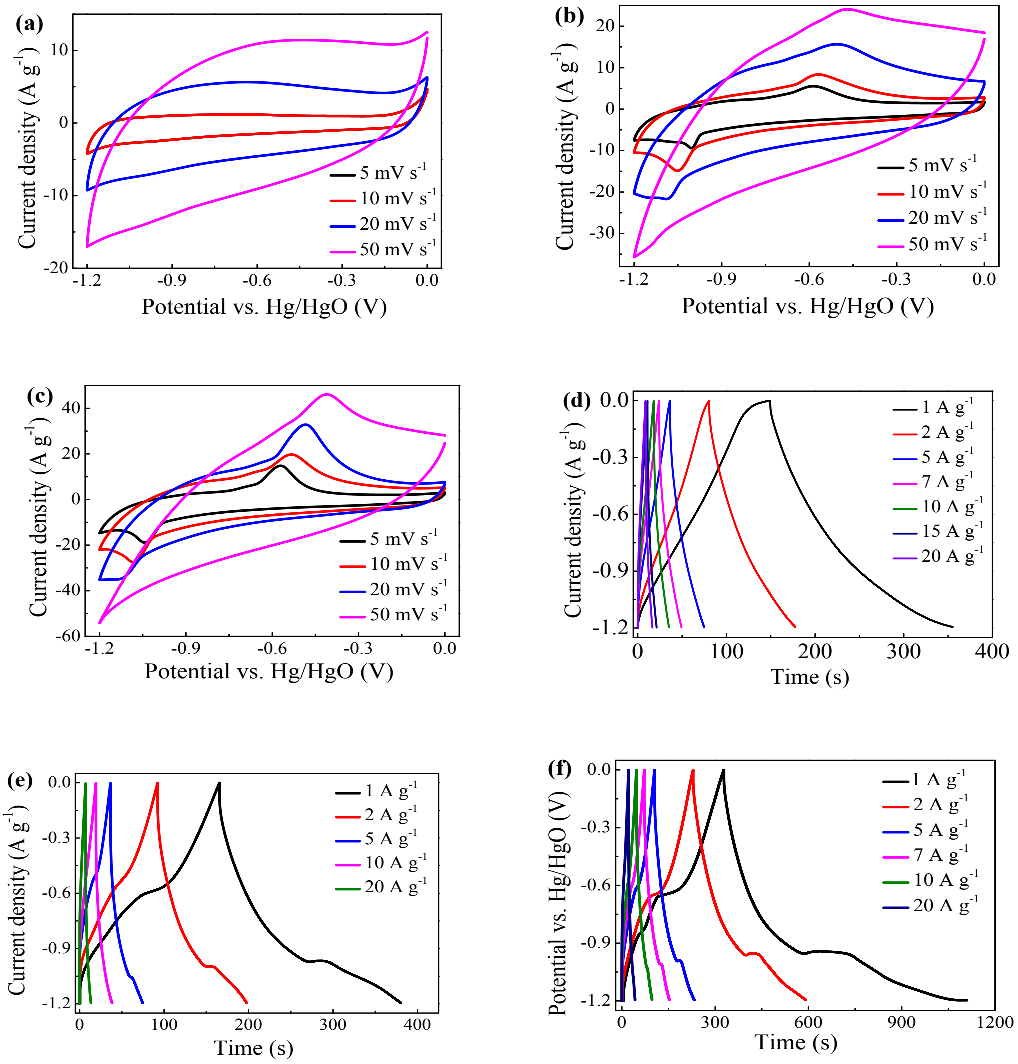

Fig. S25. CV curves of (a) f-MoS_2, (b) Fe_2O_3 and (c) MoS_2-Fe_2O_3 at different scan rates. Galvanostatic charge/discharge curves of (d) f-MoS_2, (e) Fe_2O_3 and (f) MoS_2-Fe_2O_3 at different current densities. The MoS_2-Fe_2O_3 hybrids show the largest loop area, indicating their superior electrochemical capacitive performance compared with neat f-MoS_2 and Fe_2O_3. The f-MoS_2 has a rectangular shape, while there is a pair of anodic and cathodic peaks at about -0.6 and -1.05 V, respectively, in the Fe_2O_3 and MoS_2-Fe_2O_3 electrodes, which can be assigned to the redox process of reversible reaction between Fe^{2+} and Fe^{3+}, respectively. The MoS_2-Fe_2O_3 electrode presents a typical pseudocapacitive behavior with highly nonlinear charge/discharge curves.

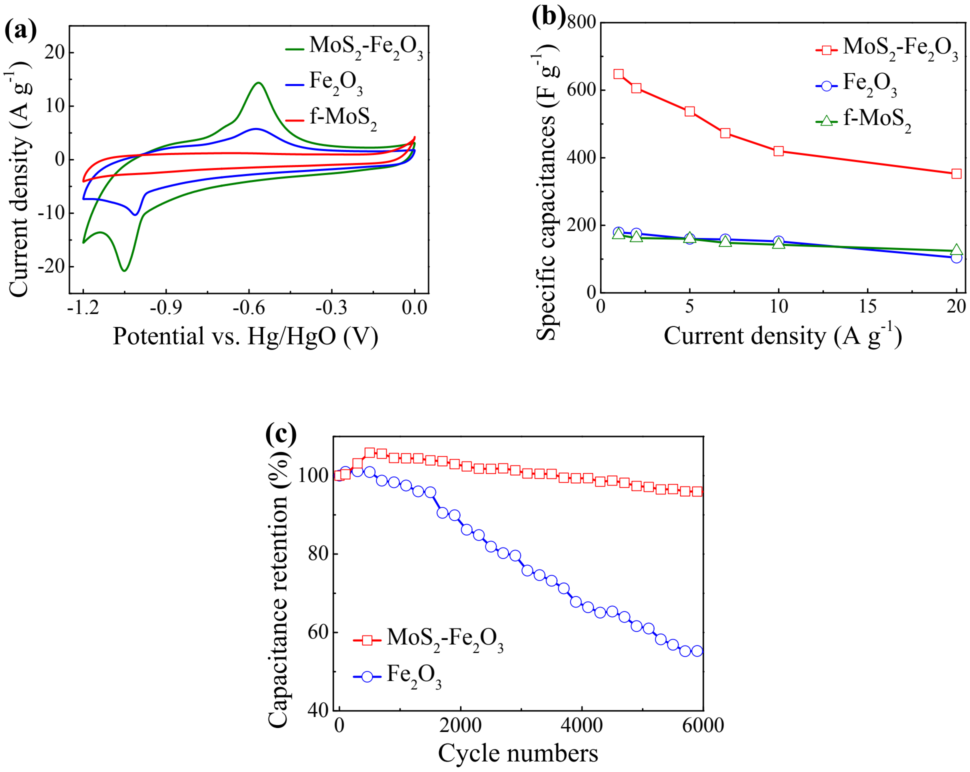

Fig. S26. (a) Comparison of CV curves of MoS_2-Fe_2O_3, Fe_2O_3 and f-MoS_2 at a scan rate of 5 mV s^{-1}. (b) Specific capacitances of MoS_2-Fe_2O_3, Fe_2O_3 and f-MoS_2 at various current densities. (c) Cycling performance of MoS_2-Fe_2O_3 and Fe_2O_3 at a current density of 2 A g^{-1}. The specific capacitances of MoS_2-Fe_2O_3 electrodes are 647.8 and 362.5 F g^{-1} at current densities of 1 and 20 A g^{-1}, respectively, indicating an excellent rate performance exceeding neat Fe_2O_3 and f-MoS_2. The cycling stabilities of Fe_2O_3 and MoS_2-Fe_2O_3 electrodes are tested up to 6000 charge/discharge cycles. Neat Fe_2O_3 as electrode materials can hardly achieve a satisfying cycling stability, but a rational combination of f-MoS_2 and Fe_2O_3 into unique hybrids reaches a significantly enhanced cycling stability. For MoS_2-Fe_2O_3 hybrids, the capacitance retention of the MoS_2-Fe_2O_3 electrode decreases gradually to ~ 96% after 6000 cycles, while neat Fe_2O_3 electrode displays a continuous decrease to ~ 54% after 6000 cycles.

References

[S1] W. Ji, J. Ji, X. Cui, J. Chen, D. Liu, H. Deng and Q. Fu, *Chem. Commun.*, 2015, **51**, 7669.

[S2] H. Xu, C. Zhang, W. Zhou and G-R. Li, *Nanoscale*, 2015, **7**, 16932.

[S3] C. Hao, F. Wen, J. Xiang, L. Wang, H. Hou, Z. Su, W. Hu and Z. Liu, *Adv. Funct. Mater.*, 2014, **24**, 6700.

[S4] J. Zhu, W. Sun, D. Yang, Y. Zhang, H. H. Hoon, H. Zhang and Q. Yan, *Small*, 2015, **11**, 4123.

[S5] X. Wu, Q. Wang, W. Zhang, Y. Wang and W Chen, *Electrochim. Acta*, 2016, **211**, 1066.

[S6] J. Cheng, B. Zhao, W. Zhang, F. Shi, G. Zheng, D. Zhang and J. Yang, *Adv. Funct. Mater.*, 2015, **25**, 7381.

[S7] H. Yi, H. Wang, Y. Jing, T. Peng and X. Wang, *J. Power Sources*, 2015, **285**, 281.